

Electron paramagnetic resonance calculations for hydrogenated Si surfaces

M. Rohrmüller,* W. G. Schmidt, and U. Gerstmann

Lehrstuhl für Theoretische Materialphysik, Universität Paderborn, 33095 Paderborn, Germany

(Received 10 January 2017; published 17 March 2017)

Electron paramagnetic resonance (EPR) signatures, more specifically the elements of the electronic g tensor, are calculated within density functional theory for hydrogenated Si(111), Si(001), Si(113), Si(114), Si(11 $\bar{2}$), and Si(110) surfaces. Thereby both perturbation theory and a more sophisticated Berry phase technique are applied. Specific defects on different surface orientations are shown to reproduce the resonances at $\bar{g} = 2.0043$ and $\bar{g} = 2.0052$ measured for hydrogenated microcrystalline silicon: The latter value is argued here to originate from regions with low hydrogen coverage; the resonance at $\bar{g} = 2.0043$ is shown to appear in positions with dihydride environment, where an H atom is directly bound to the silicon dangling-bond atoms. A third group of EPR signals with considerably larger \bar{g} values between 2.006 and 2.009 is predicted for highly symmetric dangling bonds resembling single dangling-bond defects in silicon bulk material. As the exact value depends strongly on local strain, this type of defect can explain a less intense signal with large g strain observed in microcrystalline as well as in amorphous material.

DOI: [10.1103/PhysRevB.95.125310](https://doi.org/10.1103/PhysRevB.95.125310)**I. INTRODUCTION**

There has been a long-standing and growing interest in the electrical, structural, and optical properties of hydrogenated nanocrystalline and microcrystalline ($\mu\text{c Si:H}$) silicon [1,2]. This interest is fueled largely by the promises of $\mu\text{c Si:H}$ for thin-film solar cell development. The material enables the (low-cost) fabrication of large area thin-film structures at low temperatures, and, in particular, on flexible substrates using roll-to-roll processing [3]. Its complex structure comprising amorphous matrix, crystallites, pores, and interfaces is a distinctive feature of $\mu\text{c Si:H}$. It severely complicates the exploration of the relation between atomic geometry and electronic properties. Electron paramagnetic resonance (EPR) is one of the techniques frequently used to characterize $\mu\text{c Si:H}$ and related material [4]. So far, the availability of powder spectra and the still limited sensitivity of magnetic resonance spectroscopy if applied onto single surfaces prevents a resolution of Si-related hyperfine splittings. Often, only the electronic g tensor, or even its angular average \bar{g} , can be determined and remains as a basic key to identify the dominant paramagnetic defect structures. In bulk material, by comparing measured and calculated g tensors, often an assignment of spectral signatures to microscopic structural motifs is possible, see, e.g., Refs. [5–8].

In case of amorphous silicon (a-Si:H), localized defect states in the mobility gap are known to limit the performance of thin-film solar cells and other devices. The defect centers are often paramagnetic and give rise to an inhomogeneously broadened asymmetric EPR line at around $\bar{g} = 2.0050 \dots 2.0055$ [9]. Two additional, less intense signals have been recently derived from careful line shape analysis: one signal with large g strain between 2.006...2.008 and a H-related doublet around 2.0045. Both signals can also be observed in $\mu\text{c Si:H}$ material [10]. Here, two further resonances are observed at $\bar{g} = 2.0043$ and $\bar{g} = 2.0052$ [11]. Both resonances were speculated to originate from surface

related states, either from intrinsic Si dangling-bond (db) defects or from electronic states related to adsorbed species [12]. The present paper aims at assisting in the assignment of these resonances and thus in the identification of relevant $\mu\text{c Si:H}$ defect structures by density-functional theory (DFT) electronic structure and g -tensor calculations for a variety of Si:H surface orientations shown in Fig. 1. In addition to presenting numerical values for many conceivable defect structures we search for general trends that govern the relation between microscopic structural motifs and paramagnetic resonances.

Our work is organized as follows: After a brief overview of the methodology and numerical implementation we present and discuss results for a large variety of dangling-bond defects at hydrogenated silicon surfaces. Besides the Si(111) and Si(001) surfaces, well known from wafers in semiconductor technology, also the corresponding perpendicular cuts Si(11 $\bar{2}$) and Si(110) as well as stable Si(113) and Si(114) high-index surfaces are investigated. Depending on the hybridization of the db Si atoms, the structural motifs, and the H content in the

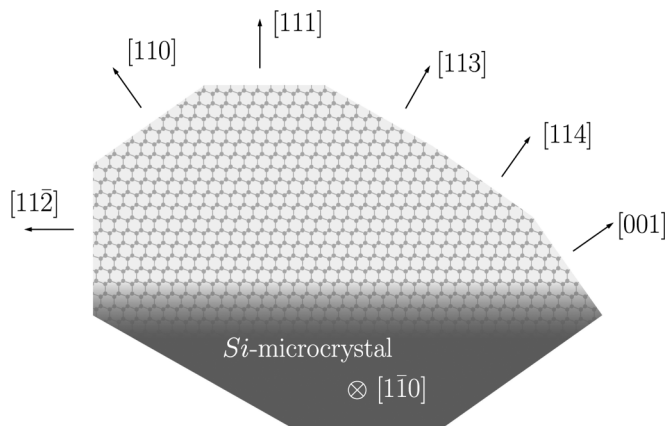


FIG. 1. Microcrystal with different surface orientations. Besides low-index surfaces, stable high-index orientations (11 $\bar{2}$), (113), (114) are indicated. Other high-index surfaces tend to faceting into low-index terraces.

*rohry@phys.uni-paderborn.de

neighborhood, we observe a three-modal \bar{g} distribution for db defects with values between 2.006 . . . 2.009 and slightly above 2.005 as well as 2.004, which can explain the experimental data observed for $\mu\text{C Si:H}$.

II. METHODOLOGY

A. g tensor definition and calculation

The definition of the electronic g tensor starts from the leading term in the phenomenological spin Hamiltonian

$$\hat{H}_{\text{spin}} = \frac{\alpha}{2} \vec{S} \cdot \underline{\underline{g}} \cdot \vec{B} \quad (1)$$

which is typically employed to describe EPR resonances. The elements of the g tensor are, thus, given as second energy derivatives with respect to the components of the magnetic field and the electron spin

$$g_{\mu\nu} = \frac{2}{\alpha} \left. \frac{\partial^2 \langle \hat{H} \rangle}{\partial B_\mu \partial S_\nu} \right|_{\vec{B}=0}. \quad (2)$$

According to Ref. [13], in the presence of a constant external magnetic field \vec{B} , one obtains the following terms up to the second order in the fine structure constant,

$$g_{\mu\nu} = g^Z \delta_{\mu\nu} + g_{\mu\nu}^{\text{Z-K}} + g_{\mu\nu}^{\text{SO}} + g_{\mu\nu}^{\text{SOO}}, \quad (3)$$

where $g^Z = g_e = 2.002\,319\dots$ corresponds to the free-electron g factor.

The Zeeman kinetic energy correction (or relativistic mass correction) gives rise to an isotropic, purely kinematic relativistic correction

$$g_{\mu\nu}^{\text{Z-K}} = -\frac{\alpha^2 g_e}{2S_{\text{eff}}} \delta_{\mu\nu} \sum_{\sigma=\pm} \sigma \langle \hat{T}_\sigma^{(0)} \rangle. \quad (4)$$

Here, S_{eff} is the total spin and $\langle \hat{T}_\sigma^{(0)} \rangle$ is the kinetic energy expectation value of the ground state with respect to the orbitals of spin channel $\sigma = \pm 1$, respectively (\uparrow and \downarrow). Usually, the relativistic mass correction provides a minor, but already for light elements non-negligible, contribution of a few percent, cf. Table I.

TABLE I. Calculated principal values of the g tensor for the prototypical, axial symmetric Si(111):H dangling-bond (db) defect (cf. Fig. 2) modeled within a $2\sqrt{3} \times 2\sqrt{3}$ unit cell using a $6 \times 6 \times 1$ k -point mesh. The Zeeman kinetic energy (Z-K), the dominating spin-orbit (SO) term, and the almost negligible spin-other orbit (SOO) contributions are given separately (in [ppm]). As a potentially more accurate alternative for g^{SO} , the contribution g^{orb} obtained via the orbital magnetization is also given (in brackets).

	g_\perp	g_\parallel
$g^Z = g_e$	2.002 319	2.002 319
$g^{\text{Z-K}}$ [ppm]	-85	-85
g^{SO} [ppm]	7 145	-1 129
(g^{orb}) [ppm]	(7 156)	(-1 130)
g^{SOO} [ppm]	5	5
g	2.009 385	2.001 111

The most relevant g tensor contribution, however, is caused by spin-orbit coupling

$$g_{\mu\nu}^{\text{SO}} = \frac{\alpha}{2S_{\text{eff}}} \left[\sum_{\sigma=\pm} \sigma \int \nabla V_{\text{eff}}^\sigma(\vec{r}) \times \vec{j}_\sigma^{(1),\mu}(\vec{r}) d^3r \right], \quad (5)$$

where $\vec{j}_\sigma^{(1),\mu}(\vec{r})$ is related to the spin current \vec{j}_σ induced by an external magnetic field $\vec{B}^\mu = B \vec{e}_\mu$ and may be expanded as

$$\vec{j}_\sigma(\vec{r}, \vec{B}^\mu) = \vec{j}_\sigma^{(0),\mu}(\vec{r}) + \vec{j}_\sigma^{(1),\mu}(\vec{r}) |\vec{B}^\mu| + \mathcal{O}(B^2). \quad (6)$$

The relevant *linear response* term can be written as

$$\begin{aligned} \vec{j}_\sigma^{(1),\mu}(\vec{r}) = & 2 \sum_o \Re \langle \varphi_{o,\sigma}^{(0)} | \hat{J}^p \hat{G}_\sigma(\epsilon_{o,\sigma}) \hat{H}^{(1),\mu} | \varphi_{o,\sigma}^{(0)} \rangle \\ & + \frac{\alpha}{2} n_\sigma(\vec{r}) \vec{B}^\mu \times \vec{r}, \end{aligned} \quad (7)$$

where $\hat{H}^{(1),\mu} = \frac{\alpha}{2} \vec{L} \cdot \vec{B}^\mu$ denotes the first order perturbation by the homogenous external magnetic field and the second, diamagnetic term ensures gauge invariance in the symmetric gauge $\vec{A}(\vec{r}) = \frac{1}{2} \vec{B}^\mu \times \vec{r}$. Finally, \hat{J}^p and $\hat{G}_\sigma(\epsilon)$ are the paramagnetic current operator and the Green's function, respectively,

$$\hat{J}^p = \frac{1}{2} (\hat{p}|r\rangle\langle r| + \hat{p}|r\rangle\langle r|) \quad (8)$$

$$\hat{G}_\sigma(\epsilon) = \sum_e \frac{|\varphi_{e,\sigma}^{(0)}\rangle\langle\varphi_{e,\sigma}^{(0)}|}{\epsilon - \epsilon_{e,\sigma}}. \quad (9)$$

In principle, the summation in the latter involves all virtual (empty) orbitals. Nevertheless, by making use of the completeness relation, it is possible to determine $\hat{G}_\sigma(\epsilon)$ by solving a linear system involving occupied states exclusively, cf. Refs. [14] and [15]. This projection onto the valence bands is beneficial to save computational costs; it increases numerical stability as well as accuracy, since it makes the approach robust against uncertainties in the energy difference between occupied and unoccupied states. The induced spin currents determine the dominating contribution to the g tensor, cf. Table I. Hence, they can be used to rationalize the deviation of the elements of the g tensor from the free-electron value g_e in a very illustrative way. Exemplarily, we show in Fig. 2 the current difference of the two spin channels calculated for the Si(111):H dangling-bond defect for an external magnetic field aligned perpendicular to the displayed plane. A more detailed discussion is given in Sec. III A.

Finally, as a many-particle correction, the spin-other orbit term g^{SOO} describes the contribution of the magnetic field induced by the current from the other electrons

$$g_{\mu\nu}^{\text{SOO}} = \frac{1}{S_{\text{eff}}} \int m(\vec{r}) \vec{e}_\nu \cdot \vec{B}^{(1),\mu}(\vec{r}) d^3r. \quad (10)$$

Here, $m(\vec{r}) = n_\uparrow(\vec{r}) - n_\downarrow(\vec{r})$ is the magnetization density and $\vec{B}^{(1),\mu}$ the magnetic field induced via Biot-Savart's law by the total current $\vec{j}^{(1),\mu}(\vec{r}) = \vec{j}_\uparrow^{(1),\mu}(\vec{r}) + \vec{j}_\downarrow^{(1),\mu}(\vec{r})$ corrected for self-interaction [16,17]

$$\begin{aligned} \vec{B}^{(1),\mu}(\vec{r}) = & \alpha \int [\vec{j}^{(1),\mu}(\vec{r}) - (\vec{j}_\uparrow^{(1),\mu}(\vec{r}) - \vec{j}_\downarrow^{(1),\mu}(\vec{r}))] \\ & \times \frac{\vec{r} - \vec{r}'}{|\vec{r} - \vec{r}'|^3} d^3r. \end{aligned} \quad (11)$$

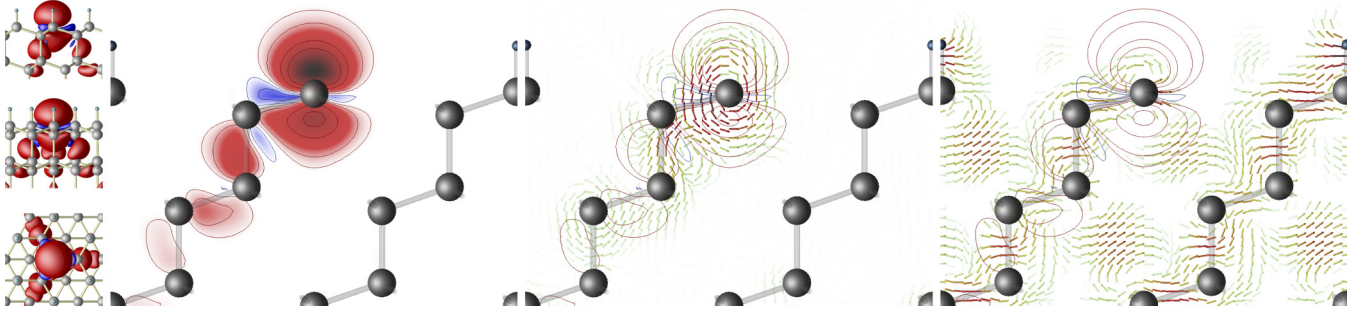


FIG. 2. Hydrogenated Si(111):H surface with a single H vacancy. Left: atomic structure (Si large, H small) and isosurfaces of the magnetization density $m(\vec{r}) = n_{\uparrow}(\vec{r}) - n_{\downarrow}(\vec{r})$. The main part [$m(\vec{r}) > 0$ red, $m(\vec{r}) < 0$ blue] is located at the unsaturated dangling bond Si atom. There are three fluctuations of $m(\vec{r})$ along the zigzag bond directions into the crystal. Calculated current density difference $\vec{j}_{\uparrow}^{(1),\mu}(\vec{r}) - \vec{j}_{\downarrow}^{(1),\mu}(\vec{r})$ (middle) and induced magnetic field $\vec{B}^{(1),\mu}(\vec{r})$ (right), both for the external magnetic field aligned perpendicular to the displayed plane (see also text). To facilitate direct comparison, the magnetization density is indicated again by isolines.

In the lower part of Fig. 2 we show this quantity for the Si(111):H dangling-bond defect. At least for the systems studied here, the resulting spin-other-orbit contributions are two orders of magnitude lower than other corrections to the free-electron g factor, cf. Table I. Notice that the evaluation of the terms for systems described by periodic boundary conditions requires a gauge invariant formalism. This is ensured by using the gauge including projector augmented wave (GIPAW) method [14].

g tensor calculations via the spin currents entering Eqs. (5) and (10) are based on linear magnetic response theory. Thereby both the influence of the magnetic field \vec{B} and the spin-orbit coupling are considered small perturbations. Numerical instabilities in the calculation of the Green's function $\hat{G}_{\sigma}(\epsilon)$, cf. Eq. (9), may occur for systems with quasidegenerate states causing large energy denominators in the Green's function [16,18]. As shown by one of the present authors [16], there is an alternative approach to the calculation of the g tensor, which goes beyond linear magnetic response. It starts from the total magnetization defined as energy derivative with respect to the magnetic field

$$\vec{M} = - \left. \frac{\partial E_{\text{tot}}}{\partial \vec{B}} \right|_{\vec{B}=0} = \sum_n f_n \langle \varphi_n | - \frac{\partial \hat{H}}{\partial \vec{B}} | \varphi_n \rangle_{\vec{B}=0}, \quad (12)$$

where f_n are the occupation numbers of state φ_n . Comparing the definition of the g tensor (2) with the magnetization (12) shows that the elements of the g tensor may be obtained by the variation in \vec{M} upon a spin flip

$$\begin{aligned} g_{\mu\nu} &= - \frac{2}{\alpha} \frac{\partial M_{\mu}}{\partial S_{\nu}} = - \frac{2}{\alpha} \vec{e}_{\nu} \frac{\vec{M}(\vec{e}_{\nu}) - \vec{M}(-\vec{e}_{\nu})}{S_{\text{eff}} - (-S_{\text{eff}})} \\ &= - \frac{2}{\alpha S_{\text{eff}}} M_{\mu}(\vec{e}_{\nu}) \\ &= g_e \delta_{\mu\nu} + g_{\mu\nu}^{\text{Z-K}} - \frac{2}{\alpha S_{\text{eff}}} M_{\mu}^{\text{orb}}(\vec{e}_{\nu}). \end{aligned} \quad (13)$$

Here, we took advantage of the fact that the total magnetization can be divided into the spin magnetization caused by the Zeeman terms and the orbital part caused by spin-orbit coupling. In this sense, the last term labeled g^{orb} substitutes for the g^{SO} term but requires by construction the evaluation of occupied states exclusively. For finite systems it can be easily

evaluated via

$$\vec{M}^{\text{orb}} = \frac{\alpha}{2} \sum_n f_n \langle \varphi_n | \hat{r} \times \hat{v} | \varphi_n \rangle, \quad (14)$$

where the velocity operator is given by the commutator $\hat{v} = -i[\hat{r}, \hat{H}]$. In case of periodic systems, however, the position operator is not well defined; a problem which can be coped with by using a Berry phase formula [19,20]. By inserting SO including wave functions the approach via the orbital magnetization goes beyond linear response and circumvents perturbation theory [7,16,18]. Provided that the contribution of the spin-other orbit term is almost negligible, which is the case for the present systems under study (cf. Table I and Ref. [21]), the two approaches lead essentially to the same results, with deviations clearly smaller than 1×10^{-5} . Based on this finding and the verified robustness of both methodologies applied here, we present the SOO term including results of the linear magnetic response method throughout the rest of this paper.

B. Numerics

The present calculations are based on the QUANTUM-ESPRESSO [22] implementation of the density functional theory (DFT). The PBE functional [23] is used to describe the electron-electron interaction within the generalized gradient approximation (GGA). The DFT band-gap problem, i.e., the underestimation of the unoccupied-states energies, is irrelevant for our g -tensor calculations. Both applied methods rely on occupied states exclusively; the Berry phase approach by construction and the linear magnetic response by taking advantage of the completeness relation. The Si surfaces are modeled within the supercell approach, i.e., finite material slabs decoupled along the surface normal by a vacuum region. Norm-conserving Troullier-Martins pseudopotentials [24] are used to describe the electron-ion interaction. The electron states are expanded in plane-wave basis, ideally suited for periodic boundary conditions.

Convergence tests with respect to slab thickness, Brillouin zone (BZ) sampling, and plane-wave energy cutoff necessary to obtain converged g tensors were performed using a paramagnetic dangling bond at the Si(111):H surface, cf. Fig. 2. Using convergence criteria $\leq 2.6 \times 10^{-3} \frac{\text{eV}}{\text{\AA}}$ and $\leq 1.36 \times 10^{-4} \text{ eV}$ for atomic surface forces and energies,

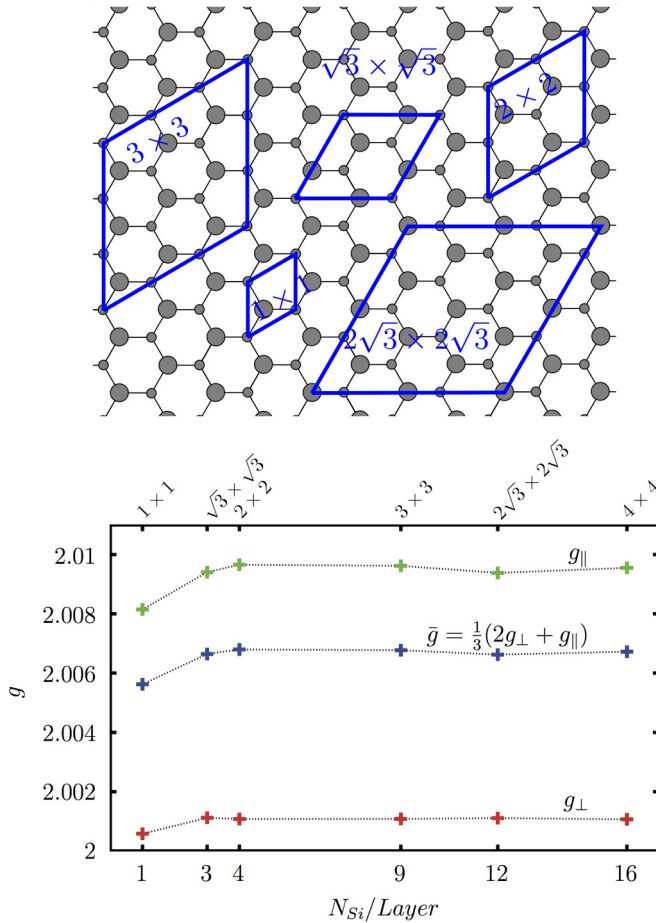


FIG. 3. Calculated g tensor components (bottom) for various surface unit cells (indicated above) used to model the prototypical Si(111):H dangling-bond defect.

respectively, six freely relaxed Si layers are found to be sufficient to properly describe the Si(111):H structure and total energy. However, 10 layers are needed to converge the g tensor within 1×10^{-4} , i.e., the typical experimental accuracy. Concerning the vacuum region, we find 10 Å sufficient for fully converged results. These calculations were performed for various plane-wave energy cutoffs. It is found that 30 Ry ensure well-converged structural and electronic properties. The g tensor calculation (via both linear magnetic response as well as Berry's phase) requires slightly denser k -point meshes than typical DFT total-energy calculations. In case of the Si(111) dangling bond modeled within a comparatively small $\sqrt{3} \times \sqrt{3}$ unit cell, we find an $8 \times 8 \times 1$ mesh necessary for the Brillouin zone sampling; for larger cells smaller k -point samplings are sufficient, e.g., $4 \times 4 \times 1$ for a $2\sqrt{3} \times 2\sqrt{3}$ cell.

The surface defect-defect interaction can potentially lead to a slow convergence with respect to the lateral unit cell size. In order to explore this issue, we modeled the Si(111):H dangling bond within a 1×1 , $\sqrt{3} \times \sqrt{3}$, 2×2 , $2\sqrt{3} \times 2\sqrt{3}$, and 4×4 surface unit cells, cf. Fig. 3. It can be seen that the calculated g tensors converge rapidly with cell size. It needs to be mentioned here, however, that this is partially related to the high symmetry of this particular defect. Defects with lower symmetry may induce long-ranging lateral strain fields

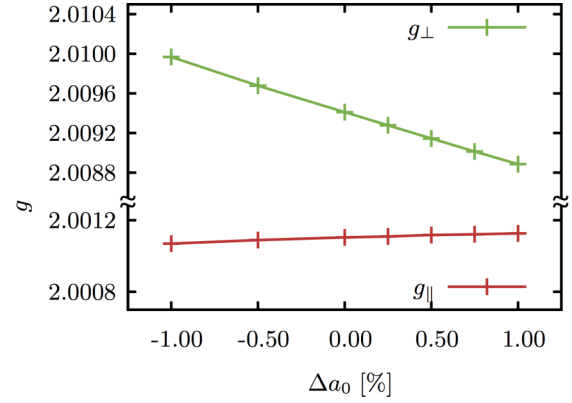


FIG. 4. Si(111):H dangling-bond defect: g tensor components calculated for strain. Whereas the component $g_{||}$ parallel to the surface normal appears quite robust, the lateral components g_{\perp} depend critically on the strain.

which require larger unit cells for an adequate modeling. One might expect the Si lattice constant entering the calculations to influence the calculated g tensor in a similar way. The present calculations are performed using a relaxed Si lattice parameter $a_0 = 5.461$ Å. This is about 0.5% larger than the measured value of 5.43 Å [25] and reflects the slight bond strength underestimation typical for the GGA. We find the g tensor components to depend nearly linearly on the lattice constant (see Fig. 4). The absolute magnitudes of the respective changes are, however, below 6×10^{-4} per percentage strain for the g_{\perp} and 0.3×10^{-4} for $g_{||}$. Whereas the latter is negligible, the influence of strain onto the lateral g tensor components is of course critical. On the one hand, this means that great care has to be spent in the theoretical description; on the other hand, this shows that the g tensor provides a sensitive probe for local strain at surfaces and interfaces.

III. RESULTS AND DISCUSSION

A. Hydrogenated Si(111) surface

Provided the hydrogen chemical potential is sufficiently high, hydrogenation of the Si(111) surface leads to an 1×1 reconstructed Si(111):H surface where all Si surface dangling bonds (db) are saturated by H [26,27]. The stability of this surface is demonstrated by the comparatively high defect formation energy required to remove a single hydrogen

$$E_{\text{form}} = E_{\text{Si(111)}} - (E_{\text{Si(111)}}^{\text{db}} + \frac{1}{2}E_{\text{H}_2}), \quad (15)$$

which we determine to be 1.14 eV, considering a $2\sqrt{3} \times 2\sqrt{3}$ surface unit cell. Hydrogen removal results in an unsaturated, singly occupied db, i.e., in a paramagnetic defect. The corresponding magnetization density is shown in Fig. 2. Mainly localized at the db Si atom, there are also spin polarization fluctuations along the three back bonds that point into the Si bulk. The sp^3 hybridized db in form of a tripod points into the [111] direction. Its C_{3v} symmetry is reflected in an axial-symmetric g tensor, which is, thus, completely characterized by its components parallel and perpendicular to the surface normal, $g_{||}$ and g_{\perp} , respectively.

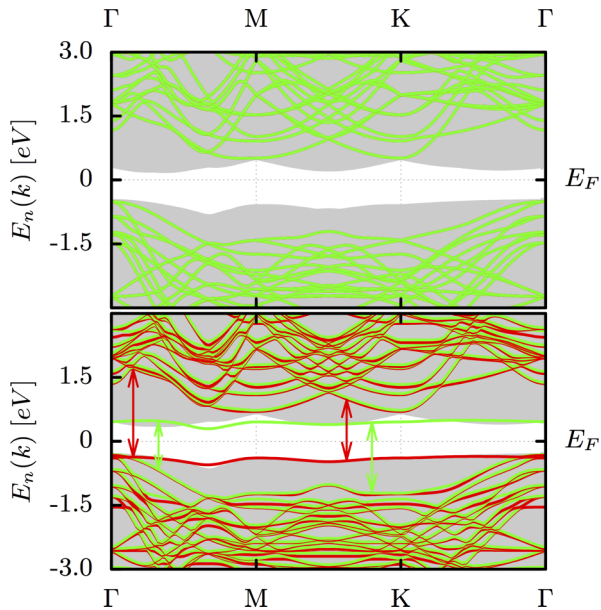


FIG. 5. Band structures calculated for the Si(111):H $2\sqrt{3}\times 2\sqrt{3}$ surface, completely hydrogenated (top) and with a single db defect (bottom); spin up/down indicated in red/green. Transition energies entering the Green's function calculation are exemplarily indicated, see text. The gray background is the surface projected Si bulk band structure.

The corresponding band structures for the fully hydrogenated Si(111):H surface, and an isolated Si(111) db defect, calculated within a $2\sqrt{3}\times 2\sqrt{3}$ unit cell are shown in Fig. 5. In the former case spin up and down bands are degenerate, while there is a clear spin splitting for the defect structure, due to the odd number of electrons. The first occupied (red, spin up) and unoccupied (green, spin down) defect bands below and above the Fermi energy E_F show almost no dispersion. This is indicative for a weak defect-defect interaction and for strongly localized defect states. Since their energies enter the denominator of the Green's function (9), this explains the rapid convergence of the calculated g tensor discussed in Fig. 3.

In Table I the calculated g tensor for the Si(111):H db defect is decomposed into the different terms contributing to the deviation from the free-electron value g_e . Obviously, the main contribution and noteworthy the full anisotropy of the g tensor are caused by the spin-orbit term. A striking feature is a large g_{\perp} value, indicative for a strong spin-orbit splitting in the surface plane, reminiscent of the Rashba effect [28]. As we will see in the following, the Si(111):H db defect provides a prototype example which can also be found in slightly modified, less symmetric form at various Si surfaces with different orientations. However, with angular average values above 2.006, this type of dangling bond cannot explain the dominant signals at 2.0043 and 2.0052. Instead, it provides an explanation for the less intense signals with large g strain between 2.006 and 2.008, which can be observed in μc Si and a-Si:H [10]. It is also reminiscent for single dangling-bond defects in silicon bulk material [29,30]. We will come back to this point later.

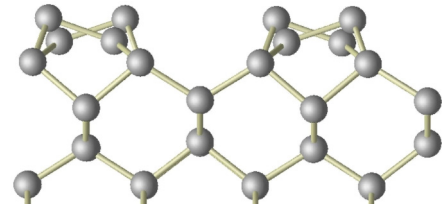


FIG. 6. Side view of the clean Si(001) $c(4\times 2)$ surface shown along the dimer rows. The alternating buckling of the Si-Si dimers can be clearly seen.

B. Hydrogenated Si(001) surfaces

Clean Si(001) surfaces reconstruct due to the dimerization of the topmost atoms. The dimers are asymmetric, consisting of an sp^2 -like bonded down atom, which moves closer to the plane of its three nearest neighbors, and an up atom, which moves away from the plane of its neighbors and possesses a p -like dangling bond. The process of rehybridization is accompanied by a charge transfer from the down to the up atom. To minimize the electrostatic energy and to relieve local stress, the direction of buckling alternates within the dimer rows. The registry of buckling in neighboring dimer rows is phase shifted, such that the Si(001) surface ground state reconstructs $c(4\times 2)$ [31], see Fig. 6. Hydrogenation of this surface leads to monohydride Si(001)(2×1):H and dihydride Si(001)(1×1):H surfaces, depending on the hydrogen chemical potential [32–34].

Starting either from the ideal clean Si(001) $c(4\times 2)$, the homogeneous monohydride (*MH*) Si(001) $c(2\times 1)$:H or the completely saturated dihydride (*DH*) Si(001)(1×1):H surfaces, various defect structures were obtained by saturating and creating Si dangling bonds, see Figs. 7 and 8 for schematic top views and corresponding band structures. We mention that many more local structure motifs are conceivable [31] than we are able to consider here.

In case of the structures 1–5, cf. Fig. 7, we find the unoccupied gap surface states to derive from Si dimer down atoms, as known from the clean Si(001) $c(4\times 2)$ surface [31]. The corresponding bands show a large dispersion along the J - K and J' - Γ directions and almost no dispersion along Γ - J and K - J' , which underlines the strong dimer-dimer coupling along the dimer rows. The dispersion of the filled states is less pronounced and again essentially restricted to the direction along the dimer rows. The Si-Si-H hemihydride in structure 1 is calculated here under the constraint that it is paramagnetic. If one allows for a metallic occupation, the structure relaxes into a diamagnetic ground state with half occupied metallic spin up and spin down bands, cf. Ref. [35]. The defect structures 6–9, cf. Fig. 8, are derived from the hydrogen covered surface by H abstraction; they are characterized by more localized defect states which show little dispersion.

The g tensors calculated for the defect structures 1–9 are compiled in Table II, together with the experimental values from Ref. [11]. The microcrystals in the experimentally characterized samples are randomly oriented. Therefore only angular averaged \bar{g} values are measured. The paramagnetic hemihydride structure 1 is unique, as its calculated angular average \bar{g} is much smaller than the free-electron value g_e , cf.

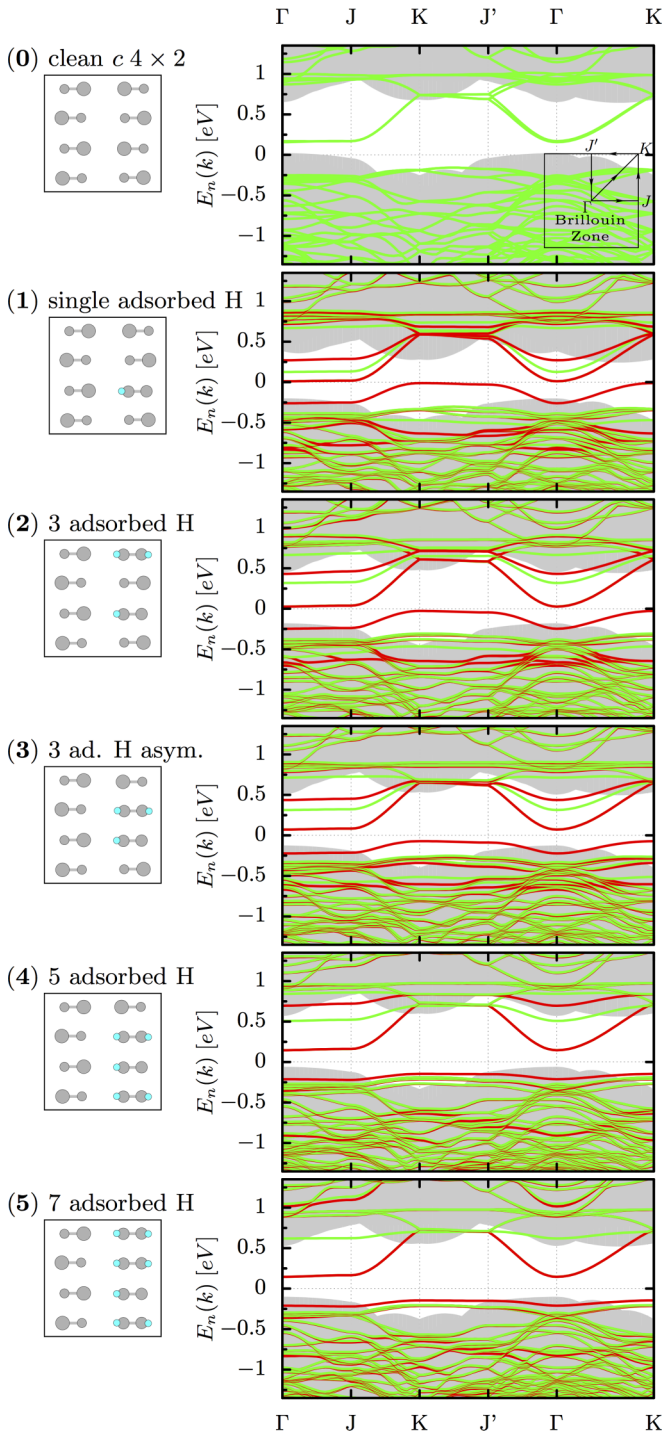


FIG. 7. Symbolic top view of Si(001):H surface supercells (left) and corresponding band structures (right), shown here for surfaces with low hydrogen coverage. The first Brillouin zone is depicted in the insert (top right). Energies are given with respect to the Fermi level; spin-up bands plotted in red, spin-down in green.

Table II. Structure 2 behaves similar, but with \bar{g} already a little larger than g_e . All other \bar{g} values presented throughout this work are considerably larger than g_e . The comparatively small \bar{g} values of structures 1, 2, and in parts also 3 can be explained by the low energy of the above mentioned strongly dispersive surface bands (representing electron states delocalized along

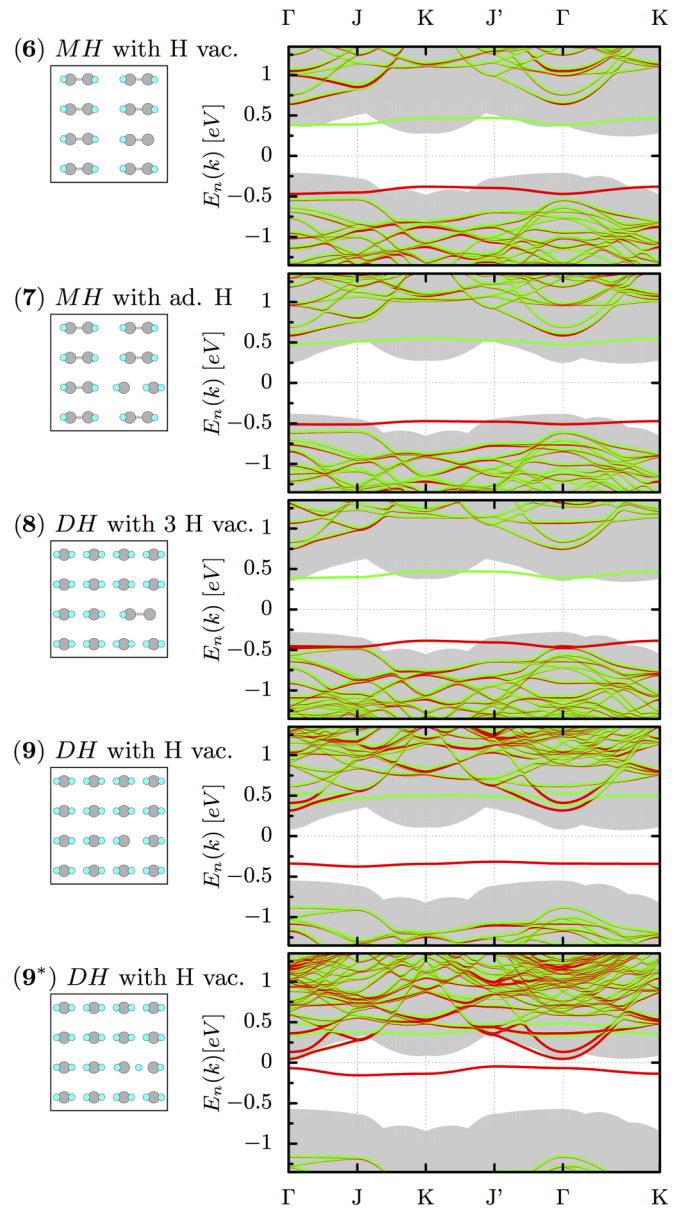


FIG. 8. Symbolic top view of Si(001) surface supercells (left) and corresponding band structures (right), shown here for structures with high hydrogen coverage, cf. Fig. 7.

the dimer). Far below the unoccupied spin-down state of the dangling bond, they result in comparatively small HOMO-LUMO gaps below 0.6 eV within the spin-down channel. In contrast to the structures with higher H coverage, these g tensors, thus, contain considerable contributions of the spin-down channel, leading to negative deviations from g_e . A prerequisite of this fingerprint is, however, a Si-Si-H hemihydride dimer embedded in a *hydrogen-free dimerized* neighborhood, in other words, a well-ordered region with minor H coverage.

Interestingly, mono- and dihydride surfaces with single missing H atoms, i.e., structures 6 and 9, give rise to \bar{g} values close to the experimental data at 2.0043 and 2.0053, respectively. The larger value at $\bar{g} = 2.0052$ can again be attributed to the Si-Si-H hemihydride structure, but now in a

TABLE II. Calculated g tensors of various Si(001) db structures in comparison to experimental values for μc -Si:H [10,11]. ϑ of g_3 is given with respect to the surface normal [001].

	\bar{g}	g_1	g_2	g_3	ϑ
1) single adsorbed H	2.000 22	1.998 24	2.002 11	2.000 30	28.6°
2) 3 adsorbed H sym.	2.002 37	1.999 17	2.002 97	2.004 97	40.9°
3) 3 adsorbed H asym.	2.003 56	2.004 28	2.005 08	2.001 33	32.8°
8) <i>DH</i> with 3 H vacancies	2.004 84	2.007 27	2.005 28	2.001 98	39.5°
6) <i>MH</i> with H vacancy	2.005 26	2.008 16	2.005 75	2.001 87	33.5°
5) 7 adsorbed H	2.005 37	2.008 25	2.005 89	2.001 97	34.4°
4) 5 adsorbed H	2.005 38	2.007 52	2.006 21	2.002 42	29.5°
expt. μc - Si:H	2.0052				
7) <i>MH</i> with adsorbed H	2.004 22	2.006 94	2.004 18	2.001 54	33.5°
9) <i>DH</i> with H vacancy	2.004 34	2.006 52	2.004 51	2.001 99	33.6°
9*) <i>DH</i> with H vacancy	2.004 54	2.006 70	2.003 79	2.003 16	41.8°
expt. μc - Si:H	2.0043				
expt. hfs(B)	2.0045	2.0056	2.0056	2.0024	

monohydride or slightly mixed mono-/dihydride environment. As illustrated in Fig. 9 (structure 6), this results in a distorted dangling bond tilted by about 32° against the surface normal. The db Si atom is still sp^3 hybridized, but the magnetization density is clearly distinct from that of the S(111):H vacancy (cf. Fig. 2). Due to surface reconstruction the prototypical tripod cannot be fully established and is reduced to a bipod; i.e., the dangling bond is built up by the p -like central part and only two fluctuations along the zigzag lines into the microcrystal.

The resonance at $\bar{g} = 2.0043$, on the other hand, requires a clearly dihydride environment. As shown in Fig. 9 (structure 9), H cleavage then might result in a sp^2 -like hybridized db Si atom and in an apparently in-plane oriented magnetization density. This alignment becomes even more obvious in structure 9*, which provides a symmetrized version of structure 9 with an adjacent H atom in a bond bridging position. The symmetric structure is energetically slightly favored by about 20 meV and provides a magnetization density which can be best explained as a kind of double dangling bond, Fig. 9 (structure 9*). The relative stability, however, depends on the details of the environment. Small inhomogeneities might lead to a symmetry break. At elevated temperatures dynamical fluctuations become possible, rendering on average the symmetric structure 9*. As can be seen from Table II, independent of a possible bistability, the underlying configuration can nicely explain the resonance at $\bar{g} = 2.0043$.

C. Hydrogenated Si(113) and Si(110) surfaces

High-index surfaces of Si tend to facet into low-index planes. Si(113) is one of a few exceptions in this respect as its surface energy is about as small as for Si(001). Our calculations for the hydrogenated Si(113) surface start from the model established by Jacobi and co-workers [36] shown in Fig. 10. It can be described as composed of (111) terraces separated by $[\bar{1}\bar{1}2]$ steps, cf. dashed lines in Fig. 10. This model is energetically favored as shown earlier by one of the present authors [37] and is in agreement with infrared [38–40] and Raman spectroscopy [41].

To create paramagnetic defects at the Si(113):H surface, we have to consider three conceivable H positions as indicated by

H1, **H2**, and **H3** in Fig. 10, top. The calculated g tensors for the three defect models are given in Table III; corresponding magnetization densities are shown in the lower part of Fig. 10. **H2** can be described as a mixture of two structures known from the Si(001):H surface. Its magnetization density resembles the bipod of structure 6, but the chemical environment is more similar to the dihydride case of structure 9. Notably, the resulting \bar{g} value of about 2.0047 reflects the average of the respective g tensors (2.0053 and 2.0043). **H3** is derived from the same sp^2 hybridized Si atom, but now with the p -like part of the dangling bond in-plane oriented. This leads to an energy lowering by 0.03 eV compared to **H2**. The magnetization density of **H3** is reminiscent of **H2**, but inverted with respect to a (110)-oriented mirror plane. Hence, both are similar to the structures 9, 9* at the dihydride Si(001):H. But the close neighborhood to the [110]-oriented step edge, separating the narrow (001) terraces, leads to increased local strain and increased g values in the [110] direction.

The most stable paramagnetic dangling bond at the Si(113):H surface, however, is related to position **H1**. The respective vacancy defect is energetically favored by about 0.2 eV. Its calculated g tensor agrees almost exactly with the calculation for the Si(111):H db defect, cf. Table I. This is not too surprising, as the chemical environment of the nearest and the next-nearest neighbor atom of the respective db are identical, and only affected by slight strain: The angle of the principal value closest to the surface normal (g_3) is 28.7° for **H1**, deviating only 0.8° from the ideal [111] direction. As shown in Fig. 10, these small deviations from the ideal symmetry are, nevertheless, visible in the magnetization density; they are, e.g., manifested in a spin polarization of two neighboring H atoms and a slightly deformed db orbital.

A similar, even more symmetric geometry is found for a dangling bond at the Si(110) surface: The clean Si(110) surface reconstructs 16×2 , forming two eight atom long (110) terraces with a step in between. Hydrogenation does not change the reconstruction pattern and leads to a configuration where the terrace Si atoms are nearly in truncated bulk positions [43]. Therefore, we model the Si(110):H surface within a (1×1) reconstruction and neglect the steps. This model structure has been shown to account reliably for the surface optical

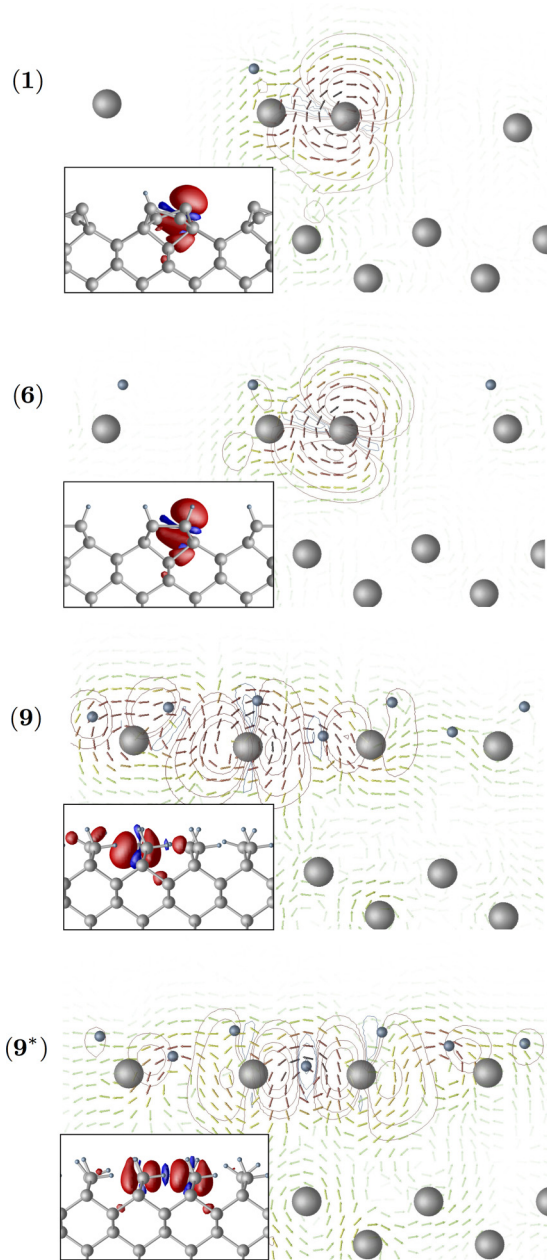


FIG. 9. Structural models, magnetization densities (insets), and induced spin currents calculated for selected defect structures from Figs. 7 and 8: **1** (top), **6** (middle); besides **9**, its symmetric ground state **9*** (bottom) is shown. For comparison and further details, see also Fig. 2 and text.

response of Si(110):H [37]. All surface adsorbed hydrogen atoms are then in equivalent configurations and there is only one possible vacancy position, at least if single vacancies are considered. The structure and the distribution of the unpaired electron is shown in Fig. 10. Again the magnetization density is very similar to that of the H vacancy at Si(111):H, already in the rather small supercell. Also the principal axis of the g tensor deviates only slightly by 1.0° from the ideal [111] direction, showing again the symmetry of the structural and chemical environment of the nearest and next-nearest neighbor atoms and in particular the lateral strain. As a result, typical

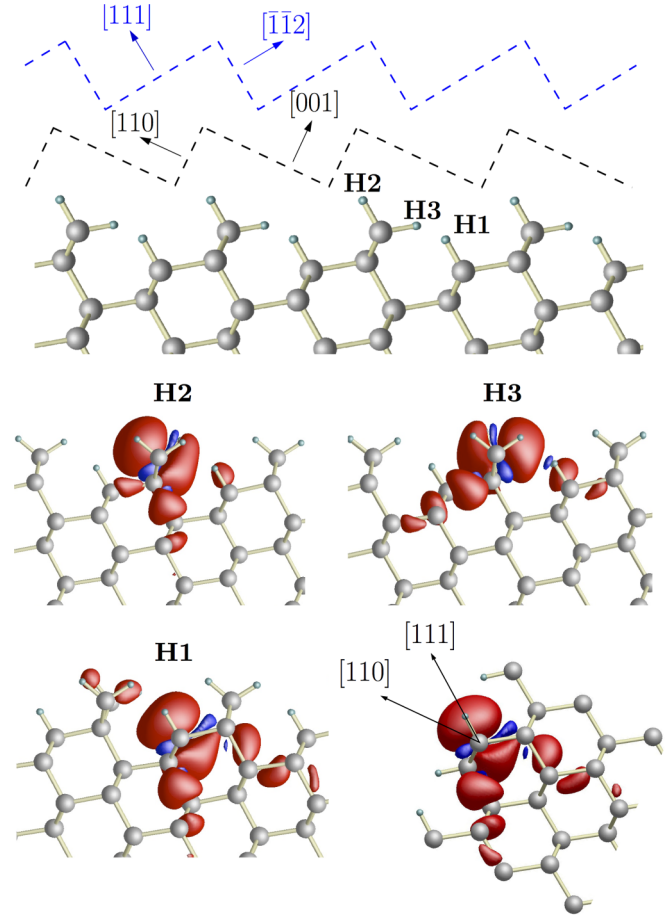


FIG. 10. Top: Structure model for ideal Si(113):H. Possible H vacancy positions are marked. The dashed lines show low-index crystal orientations. Lower parts: geometries and magnetization density of H vacancies at Si(113):H. **H2** and **H3** provide rather specific dangling bonds (middle, left/right); **H1** mimics the symmetric, tripod-like H vacancy at Si(111) (bottom, left), cf. Fig. 2. For further comparison, a respective view onto the dangling bond of Si(110):H with H vacancy [rotated by $\langle([110],[113])\rangle$] is also given (bottom, right).

tripod-like fluctuation of the spin density along the Si-Si zigzag lines into the microcrystal can be established. Nevertheless, the lateral components are by far larger than that of the Si(111):H db prototype, resulting in a quite large averaged \bar{g} value of about 2.0087. A similar observation is known from Si bulk material, where single dangling-bond defects with similar g tensor anisotropy and \bar{g} values between 2.007 and 2.010 have been observed (see also Table III). We note that increasing the lateral cell size tends to decrease the two lateral components, but only to a small amount below 1×10^{-4} .

D. Hydrogenated Si(114) and Si(11 $\bar{2}$) surfaces

The Si(114) surface is another high-index surface not subjected to faceting. Our calculations start from the 2×1 reconstruction model proposed for the clean surface by Barlow *et al.* [44]. It features a tetramer, a dimer, and two rebonded atoms. The dimer and the closed side of the tetramer buckle and also the two rebonded atoms are at different heights. Hydrogen adsorption reduces the dimer buckling as known

TABLE III. Calculated g tensors and relative formation energies of H vacancies at Si(113):H; also the Si(110):H db and Si(111):H db values are given. ϑ is given with respect to the [111] direction. For comparison, experimental data for single db defects in Si bulk materials (Si B/E) [2,29,42] is cited.

	ΔE_{form} [eV]	\bar{g}	g_1	g_2	g_3	ϑ
H2	0.20	2.004 69	2.007 31	2.004 42	2.002 34	8.4°
H3	0.17	2.004 96	2.009 52	2.003 67	2.001 70	39.5°
H1	0.00	2.006 73	2.009 15	2.009 70	2.001 34	0.8°
Si(111):H db		2.006 63	2.009 38	2.009 38	2.001 11	0.0°
Si(110):H db		2.008 77	2.011 60	2.013 30	2.001 43	1.5°
expt. Si B (bulk)		2.0071	2.0096	2.0112	2.0005	1.3°
expt. Si E (bulk)		2.0099	2.0135	2.0150	2.0012	3°

from Si(001):H; saturation with hydrogen without breaking any Si-Si bonds leads to the monohydride structure shown in Fig. 11 (left). It is characterized by eight inequivalent H atoms [45], i.e., eight conceivable vacancy positions. The calculated g tensors for the respective paramagnetic db defects are compiled in Table IV. They group into pairs with similar values which correspond to structurally similar defects and are furthermore characterized by similar relative formation energies. The lowest formation energies occur for H vacancies at Si dimers, or at the open tetramer ends, all providing average \bar{g} values similar to that of the Si(111):H prototype.

The dihydride Si(114):H surface structure shown in Fig. 11 (right) is expected for higher values of the hydrogen chemical potential. Here, six different hydrogen, i.e., dangling-bond positions **H1–H6** occur. **H3** and **H4** terminate single Si surface atoms and are quite similar to **H3/H2** at the Si(113):H surface (cf. Fig. 10), but with reduced possibilities to relax. The additional local strain leads to further enlarged \bar{g} values for the respective H vacancies, see also Table V. Comparatively large \bar{g} values are also obtained for **H1** and **H5**, both terminating threefold coordinated surface Si atoms: If these positions are dehydrogenated, the resulting dangling bonds mimic the prototypical tripod of the Si(111):H surface. Nevertheless, all these configurations provide exceptionally high formation energies and are, thus, less probable to occur. **H2** and **H6** are by about 1.6 eV lower in energy; they resemble structurally

the dihydride Si(001) dimers structure **9/9***. Hence, they offer two different configurations: (i) a metastable state with a sp^2 -like hybridized db Si atom, where the H-Si-H units are asymmetrically distorted and (ii) a (more) symmetric ground state, with one of the adjacent H atoms in a bond-bridging position. Again, both configurations provide average \bar{g} values slightly above 2.004 (cf. Table V). Like the corresponding structures at the Si(113):H and Si(001):H surface, they are, thus, expected to contribute to the experimentally observed 2.0043 resonance.

This result is corroborated by our calculations for the Si(11 $\bar{2}$) surface. It is characterized by three types of terminating hydrogen atoms, cf. Fig. 12. Two of them, **H1** and **H3**, are in (111)-like bonding configurations; their calculated g tensors (cf. Table VI) are reminiscent of that of a moderately distorted sp^3 -hybridized dangling bond. A third, **H2**, is bonded similarly as in the dihydride Si(001):H case. Similar to **H2/H6** at the Si(113) surface, along [1 $\bar{1}$ 0] they build up a row of dihydride Si atoms. A supercell, which twofold repeats the bulk periodicity as indicated in Fig. 12 (right), allows for Si dimer formation, leading to various possibilities of mixed monohydride and dihydride configurations. The g tensors calculated for a bunch of conceivable **H2** vacancy configurations are listed in Table VI. Those with a sp^2 hybridized db atom depend strongly on the termination of the neighboring Si atoms (2.0039 to 2.0049). The bond-bridging position turns out to be rather robust against changes in the chemical and structural environment, thereby reproducing the experimentally observed value of 2.0043.

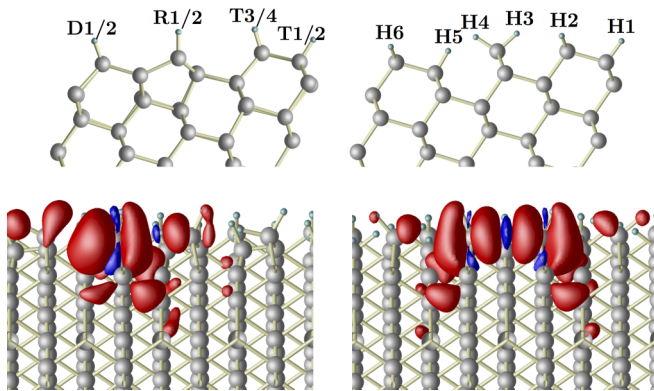


FIG. 11. Structure models for Si(114):H monohydride (top, left) and dihydride (top, right) surfaces. Possible H vacancy positions are marked. In the lower part, the spin distribution is given for the sp^2 hybridized **H2** (left) and the symmetric, bond-bridging **H2*** configurations (right), cf. Table V.

TABLE IV. Calculated g tensors and relative formation energies of H vacancies (i.e., db defects) at monohydride Si(114):H, cf. Fig. 11 (left). Dimer D1/2, rebonded R1/2 as well as tetramer positions (T1 to T4). ϑ of g_3 is given with respect to the surface normal [114].

	ΔE_{form} [eV]	\bar{g}	g_1	g_2	g_3	ϑ
R2	0.55	2.006 22	2.010 42	2.006 19	2.002 05	12.2°
R1	0.55	2.005 97	2.010 38	2.005 44	2.002 08	13.9°
T4	0.38	2.005 67	2.007 88	2.007 00	2.002 15	31.8°
T3	0.35	2.005 56	2.007 69	2.006 78	2.002 20	30.8°
T1	0.00	2.006 41	2.009 36	2.008 14	2.001 72	30.1°
T2	0.00	2.006 59	2.009 74	2.008 05	2.001 99	34.0°
D2	0.00	2.006 37	2.009 60	2.006 40	2.003 14	37.7°
D1	0.00	2.006 64	2.010 16	2.006 64	2.003 12	37.2°









TABLE V. Calculated g tensors and relative formation energies of H vacancies at dihydride Si(114):H, cf. Fig. 11 (right). The * denotes structures with an adjacent H atom in a symmetric bond-bridging position, cf. Fig. 9 (structure 9*). ϑ of g_3 is given with respect to the surface normal [114].

	ΔE_{form} [eV]	\bar{g}	g_1	g_2	g_3	ϑ
H3	1.73	2.005 30	2.008 33	2.004 96	2.002 61	44.5°
H4	1.71	2.005 16	2.009 29	2.004 52	2.001 69	65.0°
H1	1.63	2.008 20	2.012 61	2.010 56	2.001 42	38.2°
H5	1.53	2.007 20	2.009 52	2.010 92	2.001 15	35.0°
H2	0.08	2.004 03	2.002 67	2.003 53	2.005 89	29.0°
H2*	0.05	2.004 03	2.002 25	2.003 72	2.006 11	34.7°
H6	0.01	2.004 00	2.002 33	2.003 72	2.005 96	37.0°
H6*	0.00	2.004 21	2.002 99	2.003 52	2.006 11	27.6°

Judging from the robustness of the angular averaged \bar{g} values, the model with the bond-bridging H atoms serves as the most probable candidate. However, an assignment based solely on the \bar{g} value is not fully conclusive. Furthermore, the anisotropy of the g tensor is almost identical for both possible configurations as can be easily seen, e.g., in Table V for the Si(114):H surface. A distinction, in principle, would be possible via the intensity of the hyperfine (hf) splittings of the Si dangling atoms. Due to the double db character of the bond-bridging configuration, hf interactions with *two* Si db atoms are found, with hf splittings about 280 MHz, in contrast for the sp^2 -like hybridized single db configuration with values about 250 MHz. Interestingly the anisotropy is almost twice as large for the single db configurations $\approx(-70, -70, 140)$ MHz as for the double db $\approx(-40, -40, 80)$ MHz.

Further insight can be gained by the hf splittings due to the directly involved H atoms. In Ref. [10], \bar{g} values of about 2.0045 in μc -Si:H a-Si:H have been attributed to a hf-split doublet line, labeled ‘hfs(B).’ The hf splitting clearly originates from 99.99% abundant ^1H nuclei, but none of the known spectra in silicon bulk and a-Si:H material fits to this particular EPR signature. Almost all signals provide (i) much too small splittings with (ii) different symmetry (two small and one larger value). A Si-H-Si defect in silicon bulk [46] can roughly explain the hf splitting, but its g tensor is completely different ($\bar{g} \approx 1.999$) [47]. As shown in Table VII, H atoms in bond-bridging Si-H-Si configurations provide exceptionally large ^1H hf splittings in general, also for all investigated surface orientations, thereby nicely agreeing with the experimental

TABLE VI. Calculated g tensor of the H vacancies at Si(11 $\bar{2}$):H schematically shown in Fig. 12 ϑ of g_3 is given with respect to the surface normal [11 $\bar{2}$]; see text for further details.

	\bar{g}	g_1	g_2	g_3	ϑ	
	H3 vac.	2.007 96	2.012 31	2.010 57	2.000 98	20.9°
	H1 vac.	2.007 86	2.011 58	2.010 71	2.001 29	21.8°
	H2 vac. monohy.	2.006 20	2.009 50	2.006 67	2.002 44	39.8°
	H2 vac. dihy./dimer.	2.005 69	2.009 28	2.005 65	2.002 15	39.7°
	H2 vac. monohy.	2.004 89	2.009 26	2.003 64	2.001 78	27.9°
	H2* ad H monohy.	2.004 22	2.004 57	2.004 28	2.003 80	20.2°
	H2 vac. dihy.	2.004 13	2.006 21	2.003 51	2.002 68	44.3°
	H2 vac. dihy.	2.003 86	2.005 23	2.004 44	2.001 90	31.6°

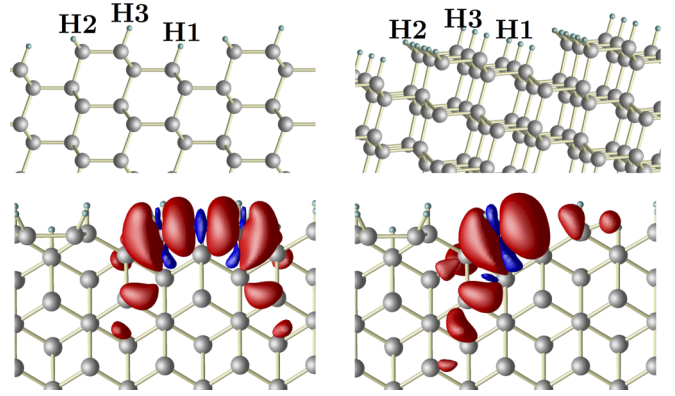


FIG. 12. Schematic views of the Si(11 $\bar{2}$):H surface with possible vacancy positions indicated (top). In the lower part, the spin distribution is given for the sp^2 hybridized **H2** (right) and the symmetric, bond-bridging **H2*** configurations (left).

hf tensor [48]. Our DFT calculations further show that the corresponding g tensor is shifted towards much higher values if the Si-H-Si defect is situated at the surface (see also Table II). Based on our calculations, we thus attribute the less intense ‘hfs(B)’ signal (around 2.0045) in μc -Si:H and a-Si:H to surface-near H atoms in bond-bridging Si-H-Si positions.

IV. CONCLUSIONS

Density-functional theory calculations on a large number of H vacancy defects at hydrogenated Si surfaces were performed in order to determine the g tensors for the paramagnetic dangling-bond defect states. The calculations show that the g tensors provide highly specific signatures that probe not only the defect itself, but also very sensitively the lateral strain and the structural and chemical environment of the nearest and next-nearest atoms. The deviation of the g tensor from the free-electron g_e value is essentially determined by spin-orbit coupling effects. Zeeman kinetic energy and spin-other orbit corrections are more than one and two magnitudes smaller, respectively, for the systems considered here.

The comparison of the calculated g tensors with experimental values from microcrystalline silicon (μc Si:H) suggests that in particular hydrogen abstracted from monohydride and dihydride (001)-oriented terraces dominate the measurements: Specific defects known from the Si(001):H surface can be also identified on many other surfaces with different orientations.

TABLE VII. Calculated hyperfine tensors for H-related db defects for various surface orientations (principal values A_i given in MHz). Θ is the angle between A_3 and the direction of the dimers [110]. Only the largest HF splitting are shown, not necessarily due to the H next to the db. For comparison, the experimentally derived signature from Ref. [10] is also given.

	A_1	A_2	A_3	Θ
Si(001) 9 DH with H vac.	34.7	34.3	36.7	12.1°
Si(001) 9* DH with H vac.	-87.0	-86.1	-23.8	0.9°
Si(114) H2	25.0	36.4	22.9	47.5°
Si(114) H2*	-84.2	-83.3	-22.6	0.5°
Si(114) H6	29.4	27.0	41.3	22.2°
Si(114) H6*	-83.8	-84.5	-21.5	2.6°
Si(11 $\bar{2}$) H2 ad. H monohy.	21.6	22.0	23.9	5.3°
Si(11 $\bar{2}$) H2* ad. H monohy.	-95.2	-94.2	-31.1	0.1°
Si(11 $\bar{2}$) H2 vac. dihy.	44.1	45.4	47.3	15.4°
Si(11 $\bar{2}$) H2* vac. dihy.	-85.1	-84.2	-23.4	0.0°
exp. hfs(B)	49.1	49.1	8.4	

Thereby, they provide similar \bar{g} values which are shown to reproduce the measured resonances at $\bar{g} = 2.0043$ and $\bar{g} = 2.0052$ [11,12]. This scenario is consistent (i) with the theoretical findings of Stekolnikov and Bechstedt that the (001) plane contributes considerably to the Si equilibrium crystal shape [49], (ii) with the suggestion that single H atoms evaporate easily from monohydride dimers, and (iii) with the observation that dihydride surfaces are in reality a disordered mixture of mono- and dihydride, where the composition and the surface morphology depend on the preparation details [31].

More specifically, the larger value at $\bar{g} = 2.0052$ is expected for regions with low hydrogen coverage, resulting in a Si-Si-H hemihydride motif. Here, the essentially sp^3 -hybridized dangling bond is tilted against the (001) surface or terrace normal, such that its magnetization density is reduced to a bipod, cf. Fig. 9 (structure 6). The resonance at $\bar{g} = 2.0043$, in contrast, is shown to appear in positions with dihydride

local environment. Here, two configurations are conceivable: (i) a quite floppy structure with a sp^2 -like hybridized db Si atom bound to two Si atoms and one H atom, and (ii) a more symmetric structure, with one adjacent H atom in a bond-bridging position. Surface reconstructions with dimers in end-to-end fashion, as present, e.g., at Si(001), Si(114) (**H2/H6**), or Si(11 $\bar{2}$) (**H2**), may lead to configurations where the H atom is symmetrically placed between two Si atoms for H rich environments [50,51]. Based on the present data, both configurations are expected to contribute considerably to the resonance measured at $\bar{g} = 2.0043$. The bond-bridging configuration provides, moreover, exceptionally large H-related hf splittings which are in nice agreement with those of the 'hfs(B)' signal in a-Si:H material. This suggests surface related Si-H-Si states to be responsible for this EPR signal. A third group of EPR signals with considerably larger \bar{g} values between 2.006 and 2.009 is predicted for highly symmetric dangling bonds resembling single dangling-bonds defects in silicon bulk material. As the exact value depends strongly on local strain, this type of defect can explain the less intense signal with large g strain between 2.006 and 2.008 observed in μc -Si:H as well as in a-Si:H [10].

Besides a better understanding of the magnetic resonances in μc Si:H and a-Si:H, the present work provides a valuable data base for the future identification of specific dangling-bond defects at perfectly oriented Si surfaces. This is expected to be of particular relevance in the context of the development of electrically detected magnetic resonance in ultra-high vacuum environment (UHV-EDMR) promising sensitive *in situ* analysis of single crystalline surfaces [52].

ACKNOWLEDGMENTS

The numerical calculations were done using grants of computer time from the Paderborn Center for Parallel Computing (PC²) and the Höchstleistungs-Rechenzentrum Stuttgart (HLRS). The Deutsche Forschungsgemeinschaft (DFG) is acknowledged for financial support via SPP-1601.

-
- [1] H. Richter and L. Ley, *J. Appl. Phys.* **52**, 7281 (1981).
 [2] Z. Saleh, G. Nogay, E. Ozkol, G. Yilmaz, M. Sagban, M. Gunes, and R. Turan, *Can. J. Phys.* **92**, 713 (2014).
 [3] R. G. Sharafutdinov, V. G. Shchukin, and O. I. Semenova, *Inorg. Mater.* **48**, 445 (2012).
 [4] D. Abou-Ras, T. Kirchartz, and U. Rau, eds., *Advanced Characterization Techniques for Thin Film Solar Cells* (Wiley-VCH, Weinheim, 2016).
 [5] M. Fehr, A. Schnegg, B. Rech, K. Lips, O. Astakhov, F. Finger, G. Pfanner, C. Freysoldt, J. Neugebauer, R. Bittl *et al.*, *Phys. Rev. B* **84**, 245203 (2011).
 [6] C. Bihler, U. Gerstmann, M. Hoeb, T. Graf, M. Gjukic, W. G. Schmidt, M. Stutzmann, and M. S. Brandt, *Phys. Rev. B* **80**, 205205 (2009).
 [7] B. M. George, J. Behrends, A. Schnegg, T. F. Schulze, M. Fehr, L. Korte, B. Rech, K. Lips, M. Rohrmüller, E. Rauls *et al.*, *Phys. Rev. Lett.* **110**, 136803 (2013).
 [8] H. J. von Bardeleben, J. L. Cantin, U. Gerstmann, A. Scholle, S. Greulich-Weber, E. Rauls, M. Landmann, W. G. Schmidt, A. Gentils, J. Botsoa *et al.*, *Phys. Rev. Lett.* **109**, 206402 (2012).
 [9] M. Stutzmann and D. K. Biegelsen, *Phys. Rev. B* **40**, 9834 (1989).
 [10] O. Astakhov, R. Carius, Y. Petrusenko V. Borysenko, D. Barankov, and F. Finger, *J. Phys.: Condens. Matter* **24**, 305801 (2012).
 [11] F. Finger, R. Carius, T. Dylla, S. Klein, S. Okur, and M. Grünes, *IEE Proc.-Circuits Devices Syst.* **150**, 300 (2003).
 [12] F. Finger, R. Carius, T. Dylla, S. Klein, S. Okur, and M. Grünes, *J. Optoelectron. Adv. Mater.* **7**, 83 (2005).
 [13] C. J. Pickard and F. Mauri, *Phys. Rev. Lett.* **88**, 086403 (2002).
 [14] C. J. Pickard and F. Mauri, *Phys. Rev. B* **63**, 245101 (2001).
 [15] A. Rodriguez-Fortea, P. Alemany, and T. Ziegler, *J. Phys. Chem. A* **103**, 8288 (1999).

- [16] D. Ceresoli, U. Gerstmann, A. P. Seitsonen, and F. Mauri, *Phys. Rev. B* **81**, 060409 (2010).
- [17] U. Gerstmann, M. Rohrmüller, F. Mauri, and W. Schmidt, *Phys. Status Solidi C* **7**, 157 (2010).
- [18] U. Gerstmann, A. P. Seitsonen, D. Ceresoli, F. Mauri, H. J. von Bardeleben, J. L. Cantin, and J. Garcia Lopez, *Phys. Rev. B* **81**, 195208 (2010).
- [19] D. Xiao, J. Shi, and Q. Niu, *Phys. Rev. Lett.* **95**, 137204 (2005).
- [20] T. Thonhauser, D. Ceresoli, D. Vanderbilt, and R. Resta, *Phys. Rev. Lett.* **95**, 137205 (2005).
- [21] S. Patchkovskii, R. T. Strong, C. J. Pickard, and S. Un, *J. Chem. Phys.* **122**, 214101 (2005).
- [22] P. Giannozzi, S. Baroni, N. Bonini, M. Calandra, R. Car, C. Cavazzoni, D. Ceresoli, G. L. Chiarotti, M. Cococcioni, I. Dabo *et al.*, *J. Phys.: Condens. Matter* **21**, 395502 (2009).
- [23] J. P. Perdew, K. Burke, and M. Ernzerhof, *Phys. Rev. Lett.* **77**, 3865 (1996).
- [24] N. Troullier and J. L. Martins, *Phys. Rev. B* **43**, 1993 (1991).
- [25] N. W. Ashcroft and N. D. Mermin, *Solid State Physics* (Holt, Rinehart and Winston, New York, 1976).
- [26] H. Ibach and J. Rowe, *Surf. Sci.* **43**, 481 (1974).
- [27] T. Sakurai and H. D. Hagstrum, *Phys. Rev. B* **12**, 5349 (1975).
- [28] É. I. Rashba, *Fiz. Tverdogo Tela* **2**, 1224 (1960) [*Sov. Phys. Solid State* **2**, 1109 (1960)].
- [29] G. D. Watkins and J. W. Corbett, *Discuss. Faraday Soc.* **31**, 86 (1961).
- [30] M. Lannoo and J. C. Bourgoin, *Physica B+C* **116**, 85 (1983).
- [31] J. Dabrowski and H.-J. Müssig, *Silicon Surfaces and Formation of Interfaces* (World Scientific, Singapore, 2000).
- [32] T. Sakurai and H. D. Hagstrum, *Phys. Rev. B* **14**, 1593 (1976).
- [33] S. Ciraci, R. Butz, E. M. Oellig, and H. Wagner, *Phys. Rev. B* **30**, 711 (1984).
- [34] A. Groß, *Surf. Sci. Rep.* **32**, 291 (1998).
- [35] M. W. Radny, P. V. Smith, T. C. G. Reusch, O. Warschkow, N. A. Marks, H. F. Wilson, S. R. Schofield, N. J. Curson, D. R. McKenzie, and M. Y. Simmons, *Phys. Rev. B* **76**, 155302 (2007).
- [36] K. Jacobi, M. Gruyters, P. Geng, T. Bitzer, M. Aggour, S. Rauscher, and H.-J. Lewerenz, *Phys. Rev. B* **51**, 5437 (1995).
- [37] W. G. Schmidt and J. Bernholc, *Phys. Rev. B* **61**, 7604 (2000).
- [38] P. Jakob, Y. J. Chabal, K. Raghavachari, R. S. Becker, and A. J. Becker, *Surf. Sci.* **275**, 407 (1992).
- [39] S. Watanabe, *Surf. Sci.* **415**, 385 (1998).
- [40] S. Watanabe, *Appl. Surf. Sci.* **130-132**, 231 (1998).
- [41] M. A. Hines, Y. J. Chabal, T. D. Harris, and A. L. Harris, *J. Chem. Phys.* **101**, 8055 (1994).
- [42] G. D. Watkins and J. W. Corbett, *Phys. Rev.* **134**, A1359 (1964).
- [43] H. Ampo, S. Miura, K. Kato, Y. Ohkawa, and A. Tamura, *Phys. Rev. B* **34**, 2329 (1986).
- [44] D. E. Barlow, S. C. Erwin, A. R. Laracuente, L. J. Whitman, and J. N. Russell, Jr., *J. Phys. Chem. B* **110**, 6841 (2006).
- [45] A. Laracuente, S. C. Erwin, and L. J. Whitman, *Appl. Phys. Lett.* **74**, 1397 (1999).
- [46] C. G. Vande Walle, P. J. H. Denteneer, Y. Bar-Yam, and S. T. Pantelides, *Phys. Rev. B* **39**, 10791 (1989).
- [47] Y. V. Gorelkinskii and N. N. Nevynnyi, *Phys. B: Condens. Matter* **170**, 155 (1991).
- [48] Experimentally only the absolute values without sign can be determined.
- [49] A. A. Stekolnikov and F. Bechstedt, *Phys. Rev. B* **72**, 125326 (2005).
- [50] P. Deák, B. Aradi, J. M. Knaup, and T. Frauenheim, *Phys. Rev. B* **79**, 085314 (2009).
- [51] V. Derycke, P. G. Soukiassian, F. Amy, Y. J. Chabal, M. D. D'angelo, H. B. Enriquez, and M. G. Silly, *Nat. Mater.* **2**, 253 (2003).
- [52] T. Risse (private communication, 2017).